



Strain-Rates Dependent Constitutive Law for Crashworthiness and Parameter Sensitivity Analysis of Woven Composites

R. Lombarkia¹ · A. Gakwaya¹ · D. Nandlall² · M. L. Dano¹ · J. Lévesque¹ · P. Vachon-Joannette¹ · P. Gagnon¹ · A. Benkhelifa¹

Received: 16 July 2021 / Revised: 17 January 2022 / Accepted: 21 January 2022 / Published online: 3 March 2022
© The Author(s) under exclusive licence to AIDAA Associazione Italiana di Aeronautica e Astronautica 2022

Abstract

The prediction of dynamic crushing behavior of aerospace-grade composites is a hard challenge for researchers. At coupons scale, such behavior implies the understanding of the initiation and propagation of the elementary damage mechanisms. Many results of the research confirm that the modulus and strength of composites increases with strain-rate. This paper presents the improvement of the constitutive model UL-Crush by adding dynamic stiffness modulus and strengths. The improved tool uses new approach by updating the stiffness and the strength values depending on strain-rates. In addition, parameter sensitivity investigations were conducted to assess the specific energy absorption capabilities of different material configurations. A new on-axis compression fixture was designed and manufactured to carry out tests of plain weave fabric composites, under quasi-static (QS) and low-velocity compression using MTS Insight 100 loading frame and drop tower CEAST Instron9340 facility. Two types of cross-section geometries were used: flat-plate and Hat-Shape coupons. Four types of triggering mechanism were adopted, including saw teeth, chamfer45°, steeple and corrugated, to ensure a continuous and stable crushing mode of failure. Detailed parameter sensitivity investigations were performed, including dimension scale, stacking sequences, trigger types and strain-rates. It was shown that the crush response is strain-rate dependent, and dynamic load decreases absorbed energy, which is indicative of microstructure disintegrating. Globally, big dimension scale, corrugated trigger, [0/45/45/0] s layout and decreasing strain-rate are the parameters to enhance the energy absorption capability of composite coupons. It has been observed that the improved numerical tool UL-Crush was able to significantly capture most crush mechanisms, reasonably correlate with experiments, and give an accurate dynamic response for crashworthy structures.

Keywords Continuum damage mechanics (CDM) · Strain-rate dependency · Finite-element analysis (FEA) · Crashworthiness · Specific energy absorption (SEA)

1 Introduction

The composite materials can improve the crash survivability during a crash landing by limiting the effects of abrupt deceleration on the occupants and protecting them from injury risks. Recent advances in computer software and hardware contribute considerably to an improvement of aerospace vehicles safety. Moreover, the shortening in processing time, the usage of inexpensive computer CPU,

memory and storage, numerical simulation of crash events may present an alternative to the high cost of real crash testing, Fig. 1, including a myriad of impact conditions that must be considered [1].

Aircraft manufacturers are currently using numerical simulations in the process of designing, testing, and certifying aircraft parts such as seats, wings, and sub-cargo (Fig. 2).

The modeling of aircraft components crash mechanisms is already involved in different explicit non-linear dynamic finite-element codes such as ABAQUS, PAM-CRASH, LS-DYNA, DYNA3D, and MSC.Dytran [4], by applying Building-Block approach.

Major damage mechanisms involved in woven composite compressive load include micro-buckling, kink-bandings, fragmentation, and delamination. In general, predicting the

✉ R. Lombarkia
redouane.lombarkia.1@ulaval.ca

¹ Department of Mechanical Engineering, Université Laval,
1065 avenue de la médecine, Quebec, QC, Canada

² Canada Defence Research & Development Canada,
Valcartier, Quebec, QC, Canada

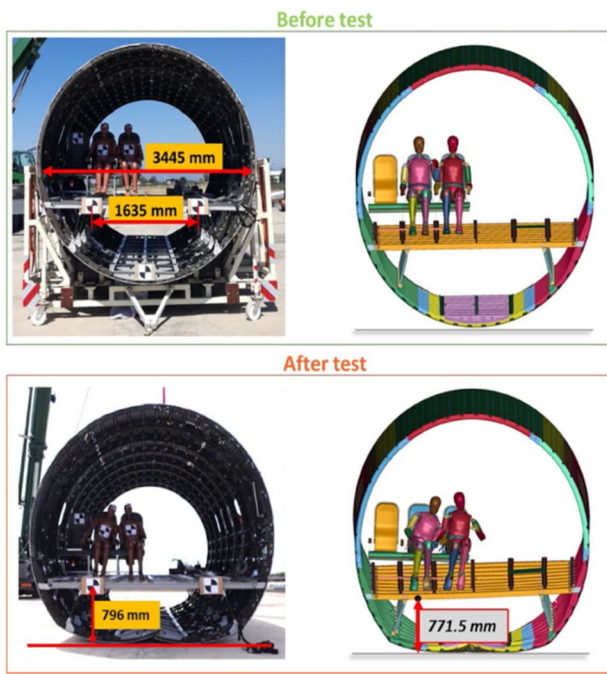


Fig. 1 Configurations before and after fuselage section crash test: experimental [2], vs numerical ($t=120$ ms) [3]

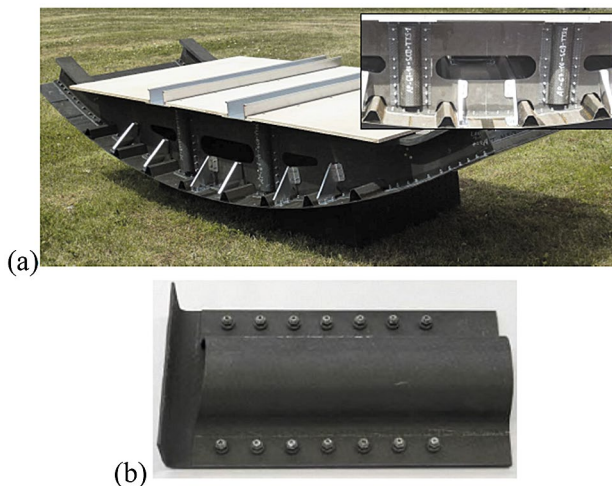


Fig. 2 **a** Sub-Cargo Demonstrator; **b** Triggered Tube Segments TTS specimen mounted on Integrated Cargo Unit ICU strut [8]

response of crash loads is even more challenging than predicting their tensile response [5–7].

At the level of coupons, correct constitutive equations are needed to predict composite material behavior under crash event.

Scale level (micro, meso, macro) and architecture of the reinforcements (UD [6, 9, 10], 2DWoven [11–13], and 3DWoven [14, 15]) are very important in modeling composites.

Micro-scale models are computation costly to model materials, Fig. 3 [15], and macro-scale models are insufficient to predict damage evolution in the material. Therefore, meso-scale models are the ideal approach compromising between numerical cost and accuracy. The meso-scale here refers to the scale of one layer of the laminate [6].

The computation costs still very advantageous for macro-models [9], but meso-scale strategy is efficient regarding industrial needs and requirements. Several other researchers used meso-mechanical-models [10, 17–19]. In the majority of existing meso-models, damage mechanisms are missing, such as kink-bandings, fragmentation and strain-rate dependency of CFRP plain weave fabric composites encountered in in-plane compression loadings [6].

For kink-bandings [20–22], a modification of the model described in [22] is performed [6]. For fragmentation, a modification of the model adopted by [23] was adapted to the crush loading of plain weave fabric composites.

For strain-rate dependency, from experimental observations, research predominantly confirms that the modulus and strength of composites increases with strain-rate and depends on the viscoelastic behavior of matrix [1, 24–26].

The composite sensitivity to strain-rate is usually driven by the non-linear behavior of epoxy matrix, which can be modeled by visco-plastic material model [2, 30]. By modeling the non-linearity of resin epoxy matrix, we allow the entire composite to behave non-linear and visco-plastically.

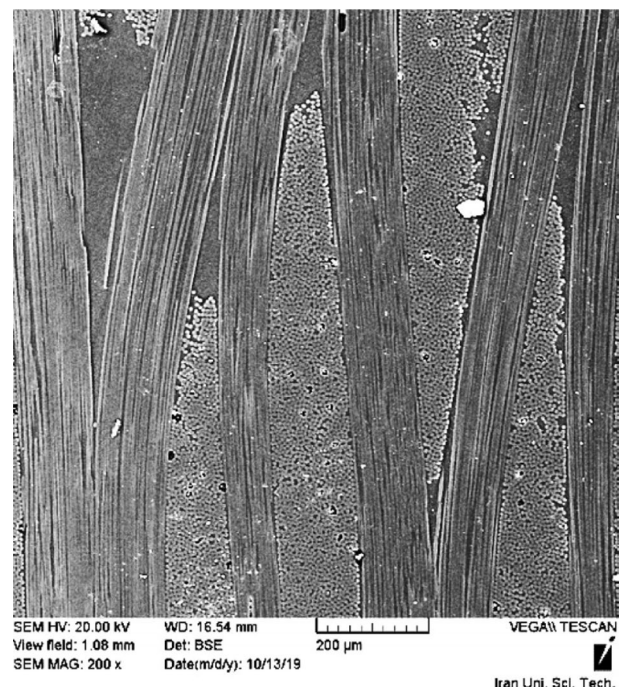


Fig. 3 Scanning electron microscope (SEM) images of the thickness of four-layer plain-woven laminate [16]

The works of [25–27] confirms the strain-rate sensitivity for the UD composite materials as well as for the woven composites in the study of [1, 28], implemented strain-rate dependent material model in micro-scale level for uni-directional composites under impact loading. Goldberg [29], developed a new model to consider the strain-rate sensitivity and the non-linear behavior of the resin by assuming a visco-plastic material model [28], includes a newly proposed fractional derivative approach implementing elastoplastic damage behavior law with strain-rate sensitivity [30], confirms the strain-rate sensitivity of elastic modulus and fracture strengths, by performing tests at strain-rates of 10^{-3} s^{-1} , 10^{-1} s^{-1} and $7 \times 10^2 \text{ s}^{-1}$ on CFRP, KFRP and GFRP specimens with a satin-weave reinforcement geometry in a polyester resin matrix [31], attributes the strain-rate effect to both the viscous behavior of the PA66 matrix and the visco-damage effect. Tests are carried out for tensile tests with a strain-rate range from the QS (10^{-4} s^{-1}) up to $3 \times 10^2 \text{ s}^{-1}$ for Twill woven carbon-polyamide laminate with three specific relative orientation of fiber: 0° , 90° and $\pm 45^\circ$, this last orientation seems to be more sensitive for strain-rate changing [32], observed during the dynamic tests, that the strain-rate effects have mainly a strong influence on the shear behavior of woven glass fiber-reinforced polyamide 66 [33], captures strain effect that was observed at higher speeds, using a spectral viscoelastic model based on a generalized Maxwell approach within a new computational model for polyamide-matrix woven composites [34], used the Northwestern Yield and Failure Criteria to provide the predictive baseline for damage propagation for strain-rate-dependent failure of a fiber-reinforced toughened-matrix composite (IM7/8552) specimens experimentally tested over the range of QS (10^{-4} s^{-1}) to dynamic (10^3 s^{-1}) strain-rates.

The formulation adopted here was initially developed by [35] and modified by [36]. Such formulation proposes a dynamic elastic modulus and dynamic strengths that accounts for the strain-rate effect.

The aim of the present work is to improve the performance of the UL-Crush material model [6]. Thus, the application of strain-rate sensitivity implies an update of the 3D Elastic modulus and strengths every time increment.

To validate the new meso-scale model and to evaluate the influence of the coupons cross-section geometries, trigger types, strain-rates and ply stacking sequences on the crushing response, experimental investigations were carried out providing relevant guidelines for future research directions. The followed methodology is described in the next section.

Section 2 provides a summary of the numerical material model and the input parameters.

Section 3 deals with the experimental procedures and coupons preparation and results measurement.

Section 4 gives results from simulations and experiments.

Finally, Sect. 5 gives summary, conclusion and outlooks.

2 Numerical Model

Elastoplastic constitutive implemented into commercial finite-element code Abaqus laws play a significant role in predicting the mechanical behavior of materials [37]. However, in some specific conditions, they cannot fit well some complex non-linear behaviors of materials such as the crushing scenarios of composite materials. A wide range of failure modes needs to be captured for the well representation of mechanical behavior, large strains, high strain-rates, coupled damage mechanisms, fragmentation, kink-bandings, etc.

Abaqus provides the ability to implement some FORTRAN user subroutines, such as VUHARD or VUMAT.

VUMAT subroutines evaluates the stress tensor at the end of increment without need of the calculation of Jacobian Matrix [38].

A new ply meso-scale material model, (Université Laval UL-Crush), is proposed, it improves and enhances capabilities of other similar material models; (Abq_Ply_Fabric, MAT_054/55, MAT_161/162, and MAT_261/262), but requires 60 input parameters with physical meaningful and relatively easy to measure.

The input parameters of the user-defined material UL-Crush are characterized in the lab and others determined from the literature [39]. The complete capabilities of UL-Crush material model can be found in details in [6].

The aim of the present work is to improve the dynamic crush response, the material model UL-Crush, which is a 3D improvement of Abq_Ply_Fabric built and embedded within Abaqus/Explicit commercial finite elements' code, to predict crush response of uni-directional UD and woven composites. This is achieved by:

- Implementing strain-rate dependency constitutive relations.

Numerical accuracy and efficiency of the improved UL-Crush numerical tool are investigated through some QS and dynamic benchmarks tests of strain-rates' sensitivity.

A. A. Strain-Rates' Sensitivity

Different formulations were proposed in the literature:

Ala Tabiei [1] developed a micro-mechanical strain-rate-dependant material model to simulate the behavior of uni-directional composites under impact loading. The strain-rate sensitivity and the non-linear behavior of the resin is

modeled by visco-plastic state variable model proposed by Goldberg [29].

Amit [40] confirms that the compression response is strain-rate dependent, which is indicative of microstructure disintegrating. In addition, the material is observed to soften as the rate of loading increases, contrary to the metals, which shows a hardening response.

Zhou [41] developed a user-defined constitutive model and strain-rate-dependant criteria and implemented within Abaqus as VUMAT subroutine with Hashin's 3D failure Criteria, to model PVC FOAM core panel reinforced by UD CFRP tubes.

Strain-rates' dependency adopted was formulated by [35, 36], and implemented in material model MAT_161/162 within Ls-Dyna finite elements' commercial code.

We assume that constitutive law is derived from the free Helmholtz strain energy which can be decomposed additively into three different contributions: elastic energy stored by the material at the point considered, and plastic energy and damage energy:

$$\psi = \psi^e(\varepsilon_{ij}^E, \phi_{ij}) + \psi^p(p, \alpha_{ij}) + \psi^d(r, \Gamma_{ij}, \phi_{ij}). \quad (1)$$

This can be written for the material at hand by

$$\left\{ \begin{aligned} \rho\psi &= \frac{1}{2}(\varepsilon_{ij}^E * (1 - \phi_{ij})\mathbf{E}^0(\varepsilon_{ij}^E) * \varepsilon_{ij}^E) \\ &+ \frac{1}{2}(H_{ij} * (\Gamma_{ij}) * H_{ij}) \\ &+ \frac{1}{2}(p_{11} * (R_{11}) * p_{11}) \\ &+ \frac{1}{2}(p_{22} * (R_{22}) * p_{22}) \\ &+ \frac{1}{2}(p_{12} * (R_{12}) * p_{12}). \end{aligned} \right. \quad (2)$$

where ρ is the density of the equivalent homogeneous material; \mathbf{E} is the plastic orthotropic stiffness matrix; \mathbf{R} is a material coefficient related to plastic hardening evolution and Γ_{ij} a diagonal matrix whose material coefficients describe the intensity of damage hardening evolution.

$(\varepsilon_p, \alpha, p, \phi, \mathbf{H}, r)$ represent, respectively, the plastic strain tensor, kinematics and the equivalent plastic strains, the damage variables, and the damage hardening variables:

$$\rho\psi^E(\varepsilon_{ij}, \varepsilon_{ij}^p, d_{ij}) = \frac{1}{2}((\varepsilon_{ij} - \varepsilon_{ij}^p)E(\phi_{ij})(\varepsilon_{ij} - \varepsilon_{ij}^p)). \quad (3)$$

With: $\varepsilon_{ij}^E = \varepsilon_{ij}$ except for: $\varepsilon_{12}^E = \varepsilon_{12} - \varepsilon_{12}^p$ & $\varepsilon_{11,22}^{cE} = \varepsilon_{11,22}^{cP} - \varepsilon_{11,22}^p$ the plastic strains.

The damaged elastic part of the free energy can be written using Gibbs formulation.

Gibbs free energy is given by

$$\left\{ \begin{aligned} \rho\chi^E &= \frac{1}{2} \left(\left(\frac{\sigma_{11+}^2}{E_{11}^0(1-\phi_{11}^+)} + \frac{\sigma_{11-}^2}{E_{11}^0(1-\phi_{11}^-)} \right) \right. \\ &+ \left(\frac{\sigma_{22+}^2}{E_{22}^0(1-\phi_{22}^+)} + \frac{\sigma_{22-}^2}{E_{22}^0(1-\phi_{22}^-)} \right) \\ &- 2 \frac{\nu_{12}\sigma_{11}\sigma_{22}}{E_{11}^0} - 2 \frac{\nu_{23}\sigma_{22}\sigma_{33}}{E_{22}^0} - 2 \frac{\nu_{31}\sigma_{33}\sigma_{11}}{E_{11}^0} \\ &\left. + \left(\frac{\sigma_{33+}^2}{E_{33}^0(1-\phi_{33}^+)} + \frac{\sigma_{33-}^2}{E_{33}^0(1-\phi_{33}^-)} \right) + \left(\frac{\sigma_{12}^2}{G_{12}^0(1-\phi_{12})} + \frac{\sigma_{23}^2}{G_{23}^0(1-\phi_{23})} \right) \right. \\ &\left. + \frac{\sigma_{31}^2}{G_{31}^0(1-\phi_{31})} \right) \end{aligned} \right. \quad (4)$$

where ρ is the density of the material, σ_{ij} are the stress components, ϕ_{ij} are the damage variables, and E^0, G^0, ν_{ij} are the pristine (undamaged) Young's moduli, shear moduli, and Poisson's ratios, respectively.

The material compliance tensor, \mathbf{S} , is then given by the second derivative of the Gibbs free energy with respect to the stress tensor:

$$\mathbf{S} = \rho \left(\frac{\partial^2 \chi^E}{\partial^2 \sigma} \right), \quad (5)$$

Strain-rates' dependency can be considered by including functions $\xi(\dot{\varepsilon}_{ij}^E)$, with $\left(\dot{\varepsilon}_{ij}^E = \frac{\partial \varepsilon_{ij}^E}{\partial t} \right)$.

The damaged elastic part of the Helmholtz free energy becomes

$$\left\{ \begin{aligned} \rho\psi^E &= \frac{1}{2}((\varepsilon_{11}^{+E}(1-\phi_{11}^+)\xi(\dot{\varepsilon}_{11}^{+E})\varepsilon_{11}^{+E}) \\ &+ (\varepsilon_{11}^{-E}(1-\phi_{11}^-)\xi(\dot{\varepsilon}_{11}^{-E})\varepsilon_{11}^{-E}) \\ &+ (\varepsilon_{22}^{+E}(1-\phi_{22}^+)\xi(\dot{\varepsilon}_{22}^{+E})\varepsilon_{22}^{+E}) \\ &+ (\varepsilon_{22}^{-E}(1-\phi_{22}^-)\xi(\dot{\varepsilon}_{22}^{-E})\varepsilon_{22}^{-E}) \\ &+ (\varepsilon_{33}^{+E}(1-\phi_{33}^+)\xi(\dot{\varepsilon}_{33}^{+E})\varepsilon_{33}^{+E}) \\ &+ (\varepsilon_{33}^{-E}(1-\phi_{33}^-)\xi(\dot{\varepsilon}_{33}^{-E})\varepsilon_{33}^{-E}) \\ &+ (\varepsilon_{12}^E(1-\phi_{12})\xi(\dot{\varepsilon}_{12}^E)\varepsilon_{12}^E) \\ &+ (\varepsilon_{23}^E(1-\phi_{23})\xi(\dot{\varepsilon}_{23}^E)\varepsilon_{23}^E) \\ &+ (\varepsilon_{31}^E(1-\phi_{31})\xi(\dot{\varepsilon}_{31}^E)\varepsilon_{31}^E). \end{aligned} \right. \quad (6)$$

The functions $\xi(\dot{\varepsilon}_{ij}^E)$ can take the following form [1]:

$$\xi(\dot{\varepsilon}_{ij}^E) = \xi(\varepsilon_{ij0}^E) \left(1 + C_{\text{rate}} \times \ln \left(\frac{\dot{\varepsilon}_{ij}^E}{\varepsilon_{ij0}^E} \right) \right), \quad (7)$$

where C_{rate} are the coefficients to regulate the dependence to the strain-rate, and ε_{ij0}^E is the reference strain-rate which is the strain-rate of the QS tests.

Dynamic elastic modulus and dynamic strengths that account for the strain-rate $\dot{\varepsilon}$ are calculated from [1]

$$E_{\text{dyn}} = E_{\text{stat}} \left(1 + C_{\text{rate}} \ln \frac{\dot{\epsilon}}{\dot{\epsilon}_0} \right)$$

$$S_{\text{dyn}} = S_{\text{stat}} \left(1 + C_{\text{rate}} \ln \frac{\dot{\epsilon}}{\dot{\epsilon}_0} \right).$$
(8)

where E_{stat} , S_{stat} are the values measured at the reference QS strain-rate $\dot{\epsilon}_0$.

B. Finite-Element Modeling

To validate the new strain-rate-dependant numerical tool UL-Crush [6], an explicit 3D crush analysis of different coupons was carried out within Abaqus/Explicit. Some simplifications are adopted to reduce the computational time. Steel solid fixed plate and steel solid translational plate are simplified to steel shells, and aluminum solid clamps are also simplified to aluminum shells. Fixed analytically rigid bodies are placed on the bottom, the friction coefficient between the coupon and the steel rigid bottom body is 0.15, and between the coupon and the aluminum clamps is 0.2.

The loading was introduced by applying a vertical constant velocity of 3 mm/min to the top steel plate for QS tests, and a vertical initial velocity of 4650 mm/s for dynamic tests.

Three different coupons geometries were performed:

(1) 1st coupon geometry: Big scale Hat-Shape cross-section

To simulate the QS crush behavior of Hat-Shape cross-section coupons, experimental and numerical investigations were conducted [42], explicit analysis was performed using Abaqus/Explicit Solver Finite-Element commercial code [43]. Coupons were modeled using 12 stacked shells, Fig. 4, by application of Abq_Ply_Fabric 2D as constitutive law. In addition, interfaces between plies were modeled using cohesive contact behavior pre-implemented within Abaqus/Explicit. $[0^\circ/90^\circ]_6$ s layup with two trigger types (chamfer45, steeple) and two coupon heights (100 mm, 150 mm) were assessed regarding the specific energy absorption.

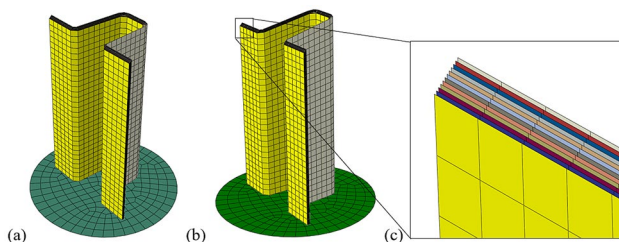


Fig. 4 Typical meshing for: **a** 45° chamfer trigger, **b** big steeple trigger, **c** 12 stacked shells

(2) 2nd Coupon Geometry: Small-Scale Hat-Shape Cross-Section

Small-scale Hat-Shape specimens were modeled [6] using solid elements C3D8R from Abaqus elements' library for plain weave fabric composite material. The models consist of four different configurations: 76.2 mm height of chamfer45 trigger and saw teeth trigger Hat-Shape open cross-section coupons with two draping: $[0^\circ/45^\circ/45^\circ/0^\circ]_s$ and $[45^\circ/90^\circ/90^\circ/45^\circ]_s$. In addition, a cohesive element COH3D8 was inserted between layers to model cohesive interfaces (Fig. 5).

(3) 3rd Coupon Geometry: Flat Plate

For the third coupon geometry, small flat plate (76.2 mm of height), modeling approach considers one layer of solid element per one real ply of laminate. Solid elements with reduced integration (C3D8R) were used to mesh the intra-composite plies. To model behavior of interface between plies, COH3D8 elements were used (Fig. 6).

Abaqus/Explicit offers Hourglass and distortion control to prevent solid elements from inverting or distorting excessively for these cases. If distortion control is used, the energy dissipated by distortion control can be output upon request [44]. UL-Crush constitutive material model was affected to the C3D8R elements.

The simulations were performed using node in Calcul-Québec Cedar supercomputer with Abaqus/Explicit and domain parallelization.

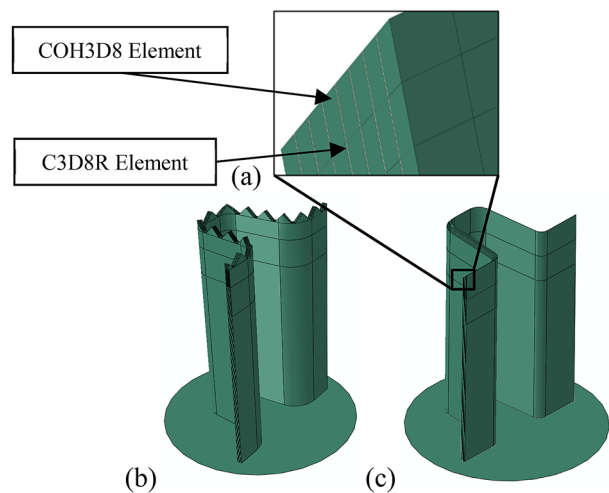


Fig. 5 Models for UL-Crush; **a** C3D8R and COH3D8 elements, **b** coupon with saw teeth trigger, **c** coupon with chamfer45 trigger

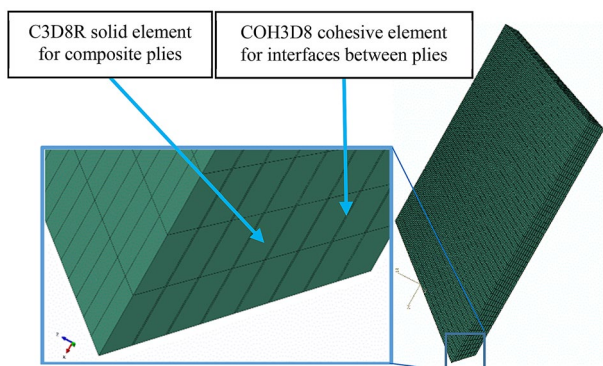


Fig. 6 Abaqus elements' type meshing for composite plies and interfaces between plies for flat-plate coupons

3 Experimental Test Plan

To assess the prediction capabilities of the new developed material model UL-Crush and to evaluate the sensibilities of multiple parameters influencing the crush behavior of woven CFRP composite materials, a systematic approach is initiated by preparing a test plan for QS and low-velocity crushes, as shown in Figs. 10 and 16, respectively.

A systematic experimental investigation is conducted to evaluate the influence of the dimension scales, trigger geometries, layups and strain-rates on the crushing response. QS and dynamic crush experiments in which one parameter is tested while keeping all other testing parameters constant are carried out. From the obtained results, the best material configuration to achieve more energy dissipation will be established.

The advanced aerospace-grade material supplied by Bell Helicopter Textron Company (BHTC) is plain weave (PW) fabric carbon fiber/epoxy prepreg. Such material is used extensively for general aviation primary structures.

A. Experimental Setup and Specimens

The used setup, Fig. 7, and specimens Fig. 9, was designed and manufactured within the M3C Laboratory, at the Mechanical Engineering Department of Université Laval. Setup is composed of two fixed plates and two vertical translational plates. An M1404 Series PCB piezo electrical Load Cell was added at the bottom of setup to capture crush forces.

Different fixtures may be added to clamp different geometries of composite coupons. A fast Camera, GOM Aramis Digital Image Correlation DIC and video extensometer have also been added to complete necessary instrumentations.

An aluminum mold was used to manufacture the Hat-Shape composite coupons.

The crush coupons were cut to the required dimensions [42, 45], to fit with the existing machines energy capacities (Fig. 8).

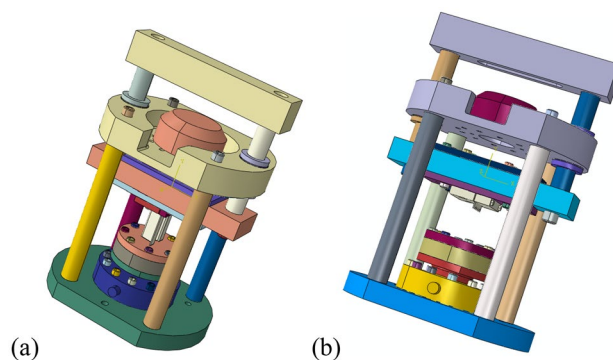


Fig. 7 New setup for crush experiments, setup for QS and Dyn crush tests to insert into enclosure cell of drop tower, **a** for Hat-Shape coupons, **b** for flat-plate coupons

Big scale Hat-Shape coupons heights are 100 mm and 150 mm with chamfer 45° and steeple trigger, with $[0^\circ/90^\circ]_6s$ layup. Unfortunately, big-scale Hat-Shape coupons are only tested for QS crush, (because of the 400 Joule maximum energy limit delivered by drop tower), and will be compared to small-scale coupons also tested for QS crush to assess the sensibility of dimension scale parameter. However, small-scale coupons are tested for both, QS and low-velocity crush, their heights are 76.2 mm with two geometry cross-sections, three layups and four trigger types [42, 45] (Fig. 9).

B. Test Campaigns

Two new test plans were prepared to validate the new constitutive law UL-Crush and to investigate the sensitivity of different parameters influencing the choice of the best material configuration absorbing and dissipating the maximum crush energy.

(1) 1st Test Campaign: QS Crush tests:

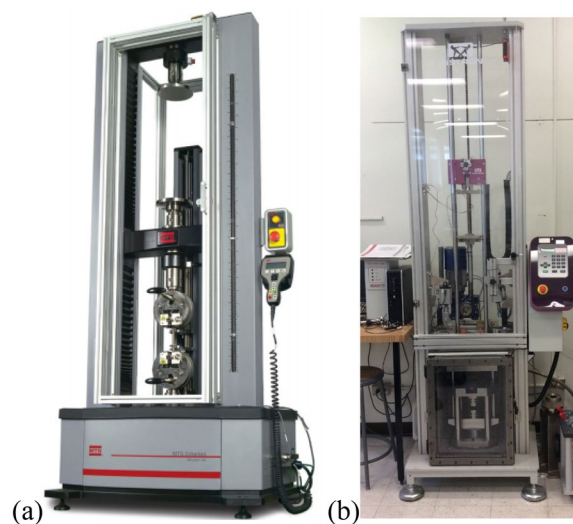


Fig. 8 **a** MTS Insight 100, **b** CEAST Instron9340 drop tower



Fig. 9 a Flat-plate coupons with corrugated trigger, b flat-plate coupon with saw teeth trigger, c Hat-Shape coupon with saw teeth trigger. d Hat-Shape coupon with chamfer45° trigger

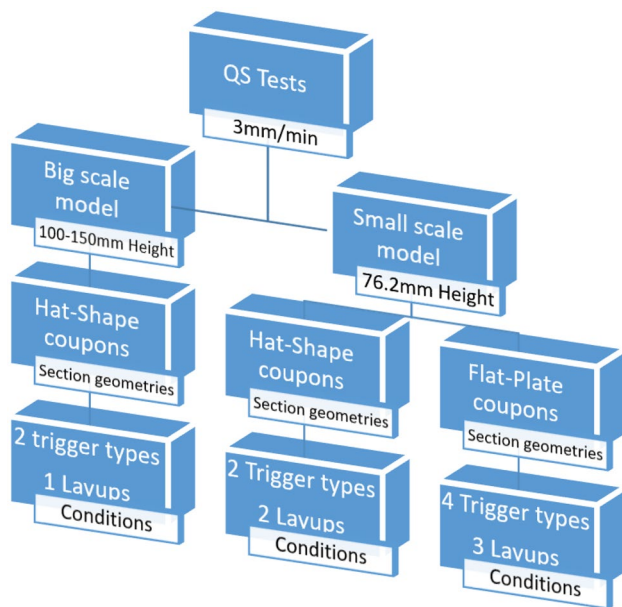


Fig. 10 Tests plan for QS CFRP plain weave fabric coupons crush

For QS tests performed at 3 mm/min, as shown in Fig. 10, two-dimension scales were adopted; big scale (100–150 mm) and small scale (76.2 mm). The specimens were then classified, first, regarding cross-section geometries: Hat-Shape or flat plate, second, regarding trigger types and layups.

Figures 11 and 12 show the post-mortem QS crush results for the big-scale and small-scale Hat-Shape coupons.

Figures 13, 14 and 15 show the post-mortem QS crush results for small-scale flat-plate coupons.

(2) 2nd Test Campaign: Dynamic Crush Tests:

For low-velocity crush tests performed at 4650 mm/s, as shown in Fig. 16, only small-scale coupons (76.2 mm) were tested, because of the energy limitation of drop tower CEAST Instron 9340 machine (400 Joule), not enough to crush big-scale coupons (100–150 mm). The specimens were then classified, first, regarding cross-section geometries: Hat-Shape or flat plate, second, regarding trigger types and layups.

Figure 17 shows the post-mortem dynamic crush results for the small-scale Hat-Shape coupons.

Figures 18, 19 and 20 show the post-mortem dynamic crush results for small-scale flat-plate coupons.

C. Parameters' Identification

As the woven fabrics have commonly a brittle linear response in the warp and weft directions, the elastic parameters such as elastic modulus and Poisson's ratio are identified following the classical ASTM standards as presented in Table 1.

For the damage identification, the Weibull function is used to describe the damage propagation.

The OCT (over-height compact tension specimen tests) were used to measure intraply strain energy release rates utilized for describing damage propagation within composite plies. Damage parameters are provided in Table 1.

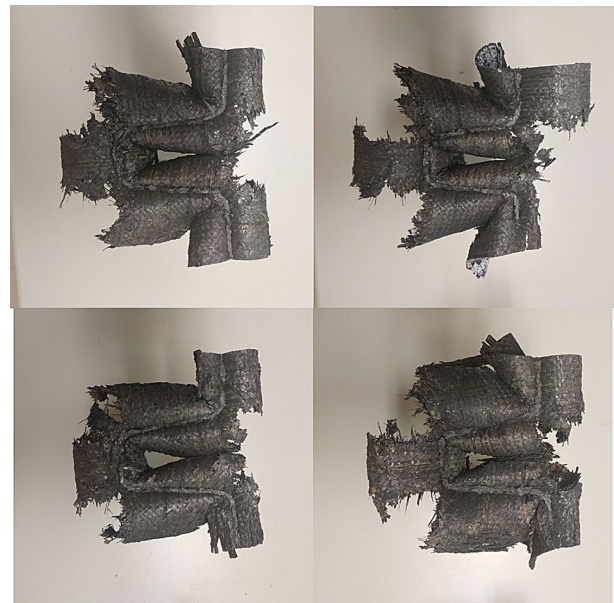


Fig. 11 Top views of QS crush tests for the big-scale Hat-Shape coupons; (top): [0°/90°]6s 150 mm with chamfer45 and steeple trigger, (bottom): [0°/90°]6s 100 mm with chamfer45 and steeple trigger

Fig. 12 Top views of QS crush tests for the small-scale Hat-Shape coupons (top): $[45^\circ/90^\circ/90^\circ/45^\circ]_s$ 76.2 mm with saw teeth and chamfer45 trigger, (bottom): $[0^\circ/45^\circ/45^\circ/0^\circ]_s$ 76.2 mm with saw teeth and chamfer45 trigger

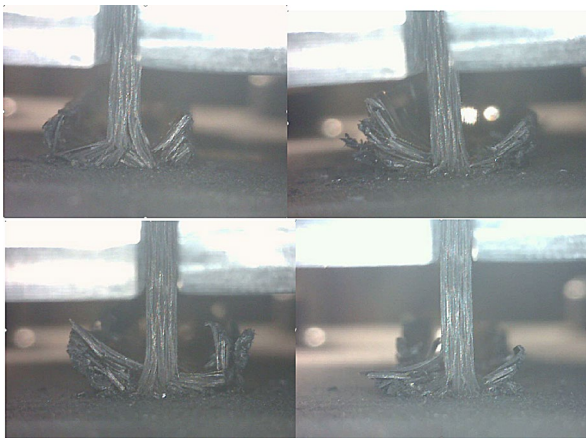
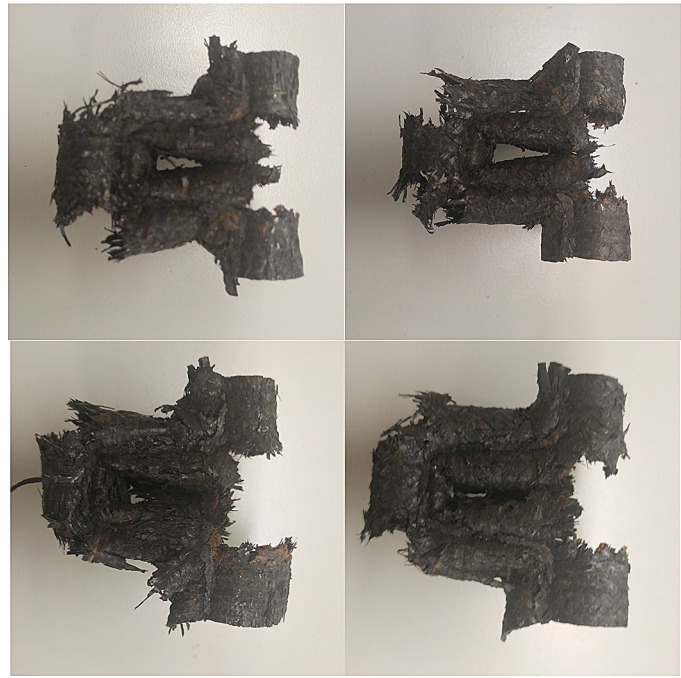


Fig. 13 Lateral views of QS crush tests results for $[0/90]_2s$ layup: (top): coupons with chamfer45° and steeple trigger, (bottom): coupons with corrugated and saw teeth trigger

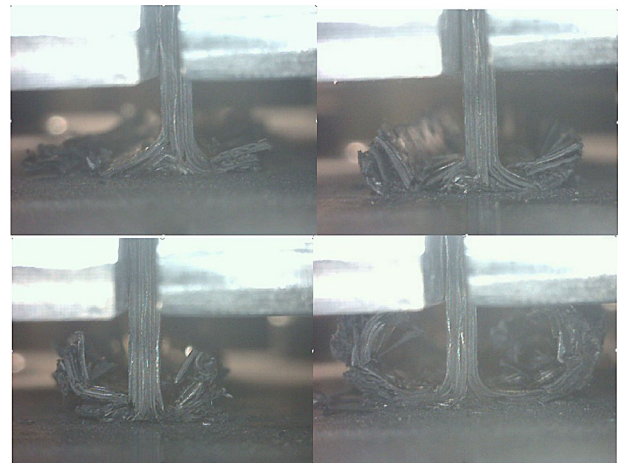


Fig. 14 Lateral views of QS crush tests results for $[0/45/45/0]_s$ layup: (top): coupons with chamfer45° and steeple trigger, (bottom): coupons with corrugated and saw teeth trigger

Typical cyclic shear tests (ASTM 3518, ASTM 2344) are used to measure in-plane shear inelasticity. The yield stress is identified from the linear regression of the elastic part in the experimental stress–strain curve. The failure stress corresponds to the maximum reached stress during the test. kink-banding failure angle corresponds to the angle of plane in which matrix failure onset implies fiber failure by kinking.

Fragmentation parameters, Table 2, are identified using new experimental strategy developed by [46]. Mean crush stress is the average stress for composite ply to create micro-fragment in crush front.

For interplay delamination, Table 2, (DCB, ENF and MMB) tests were used to identify parameters.

4 Results and Discussion

A. Hat-Shape Coupons Results

The first parameter to be evaluated is the dimension scale parameter, Table 3 shows the SEA calculated for big-scale and small-scale Hat-Shape coupons tested under QS crushing load.

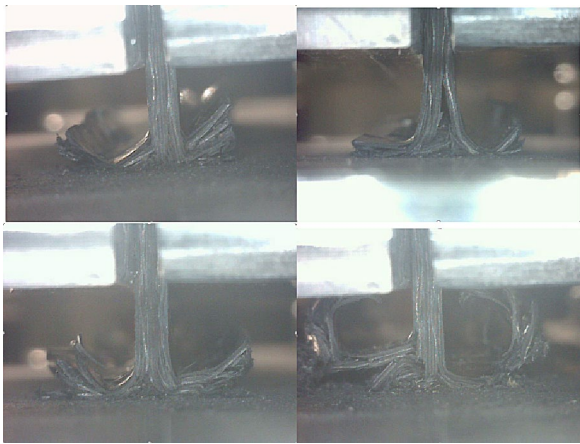


Fig. 15 Lateral views of QS crush tests results for [45/90/90/45]s layup: (top): coupons with chamfer45° and steeple trigger, (bottom): coupons with corrugated and saw teeth trigger

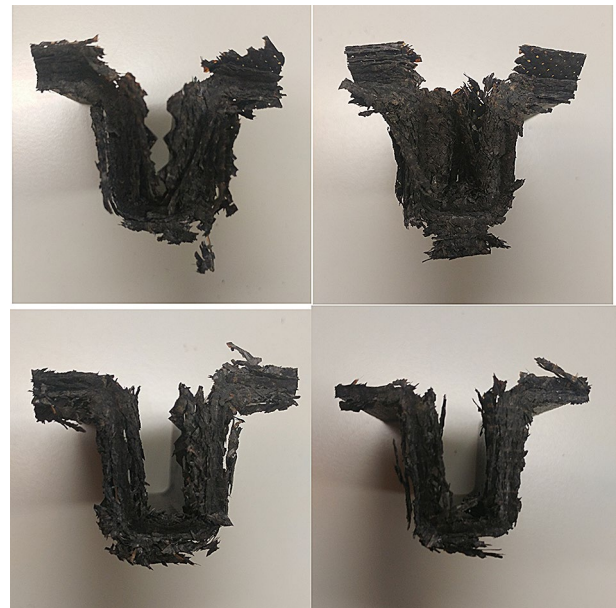


Fig. 17 Top views of Dyn crush tests for Hat-Shape coupons. (top): [45/90/90/45]s layup with saw teeth and chamfer45 trigger, (bottom): [0/45/45/0]s layup with saw teeth and chamfer45 trigger

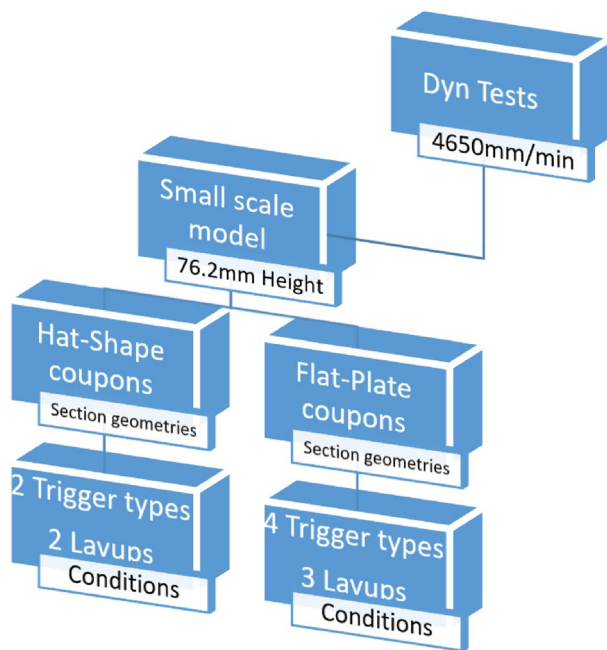


Fig. 16 Tests plan for Dyn CFRP plain weave fabric coupons crush

The big scale seems to enhance the capability of crush absorption especially for coupons with chamfer45 trigger.

Figures 21, 22 and 23 illustrate the experimental response of different Hat-Shape coupons (load vs displacement). For overall observations, the steeple and saw teeth trigger types delay the peak load response due to the height of these triggers compared to chamfer trigger. The coupons with [0°/45°/45°/0°]s layup enhance the post-peak sustained load due to the high fragmentation capability of the internal 0 degree oriented plies. Thus, enhanced post-peak load contributes to the stability and the progressive crush scenarios.



Fig. 18 Isometric views of Dyn crush tests for Hat-Shape coupons with [0/90]_{2s} layup; (top): coupons with chamfer45 and steeple trigger, (bottom): coupons with corrugated and saw teeth trigger

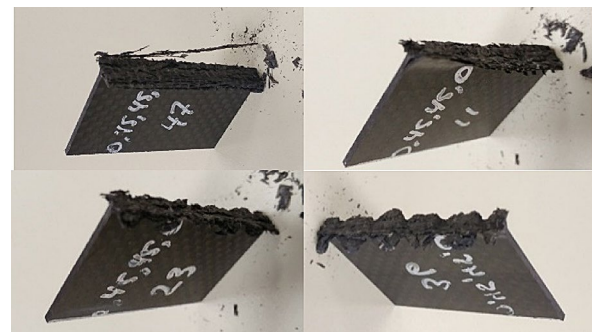


Fig. 19 Isometric views of Dyn crush tests for Hat-Shape coupons with [0/45/45/0]s layup; (top): coupons with chamfer45 and steeple trigger, (bottom): coupons with corrugated and saw teeth trigger

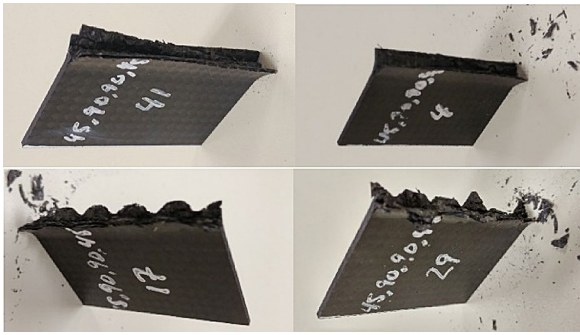


Fig. 20 Isometric views of Dyn crush tests for Hat-Shape coupons with [45/90/90/45]_s layup; (top): coupons with chamfer45 and steeple trigger, (bottom): coupons with corrugated and saw teeth trigger

The dynamic load decreases the absorbed energy because of disintegration of the internal microstructures.

Figures 24, 25, 26 and 27 show a comparison between experimental, Abq_Ply_Fabric and UL-Crush results for crushing of the small-scale Hat-Shape coupons.

The delamination, fragmentation and kink-bands were proved to be the major damage mechanisms observed during crush tests of Hat-Shape and flat-plate coupons. Fronds or petals are clearly released after delamination damage initiation followed by fragmentation and accumulation of fiber debris.

UL-Crush material model predicts well the physics of the phenomenon of crush: the first effect of crush was characterized by a force peak and associated with the first delamination onset mechanism. This effect was present for all material configurations tested. The second effect of crush was characterized by a steady-state crushing load period, which was a sign of stable and progressive crush scenario. The ratio between peak force and stable load is an important parameter to measure an excellent crush scenario leading to a maximum energy absorption to mitigate impact shock and to attenuate brutal deceleration transmitted to the passengers.

The numerical curves of Abq_Ply_Fabric and UL-Crush has an SAE600 filtering operator with 600 Hz filter applied to smooth out the numerical prediction.

For the QS crush tests, Abq_Ply_Fabric model seems to capture peak force but over-estimate the sustainable post-peak crush load. However, UL-Crush model captures well the post-peak crush load and under-estimate peak force.

For the dynamic crush tests, UL-Crush model coincides well with the peak force but slightly under-estimate the sustainable post-peak crush load. However, Abq_Ply_Fabric do not capture accurately the dynamic crush response, because no strain-rate-dependent formulation was included in such material model.

The second parameter to be evaluated is the cross-section geometry parameter; Table 4 shows the SEA

Table 1 First part: UL-Crush material model parameters' identification tests

| Parameters | Description | Identification procedures |
|------------------------------------|-------------------------------------|--|
| Ro (Kg/m ³) | Density | |
| E11t E22t (GPa) | Anisotropic elasticity | ASTM 3039 |
| E11c E22c (GPa) | | ASTM 6641 |
| E33t E33c (GPa) | | ASTM 7291 modified |
| Nu12 | | ASTM-E132 |
| Nu23 | | ASTM-E132 |
| Nu31 | | ASTM-E132 |
| G12 (GPa) | | ASTM 3518 |
| G23 (GPa) | | ASTM 2344 |
| G31 (GPa) | | ASTM 2344 |
| (Gf11t Gf11c) (kJ/m ²) | Intraply strain energy release rate | OCT (over-height compact tension specimen tests) |
| (Gf22t Gf22c) (kJ/m ²) | | |
| (Gf33t Gf33c) (kJ/m ²) | | |
| (Gf12) (kJ/m ²) | | |
| (Gf23) (kJ/m ²) | | |
| (Gf31) (kJ/m ²) | | |
| S11c S22c (MPa) | Failure onset | ASTM 6641 |
| S11t S22t (MPa) | | ASTM 3039 |
| S33t S33c (MPa) | | ASTM 7291 modified |
| S12 (MPa) | | ASTM 3518 |
| S23 (MPa) | | ASTM 2344 |
| S31 (MPa) | | ASTM 2344 |

Table 2 Second part: UL-Crush material model parameters' identification tests

| Parameters | Description | Identification procedures |
|---|---------------------------------------|---------------------------------------|
| FiZero | Kink-bandings failure angle | |
| TitaZero | Braiding angle between yarns | |
| SIGY (MPa) | In plane shear inelasticity | ASTM 3518 |
| C | | |
| P | | |
| Mean crush stress (MCS) (MPa) | Fragmentation | New experimental procedure, from [46] |
| Epsa_frag, Epsb_frag | | |
| Epsay_new, Epsby_new | | |
| n | Damage propagation | |
| Epsa_final, Epsb_final, Epsc_final, Epsab_final, Epsbc_final, Epsca_final | | |
| $C_{rate1} C_{rate2} C_{rate3} C_{rate4}$ | Strain-rates' dependency | |
| $\dot{\epsilon}_0 = \left(\frac{d\epsilon}{dt}\right)_0$ (mm/min) | Reference strain-rate | |
| GIc | Interply delamination critical energy | Mode-I: ASTM D5528-13 DCB |
| GIIc | | Mode-II: ENF, ARCAN |
| GIIIc | | Mode-III: ECT |
| (kJ/m ²) | | Mode-I+II: ASTM D6671/D6671M-13e1 |
| | | MMB |

Table 3 Calculated SEA for QS crush tests for big-scale and small-scale Hat-Shape coupons

| Layups | Triggers | Small scale Hat-Shape SEA(QS) Joule/mm ³ | Big scale Hat-Shape SEA(QS) Joule/mm ³ |
|----------------|------------------|---|---|
| [45,90,90,45]s | Chamfer45 | 0.1348 | |
| | Saw | 0.1340 | |
| [0,45,45,0]s | Chamfer45 | 0.1374 | |
| | Saw | 0.1367 | |
| [0,90]6 s | 100 mm-Chamfer45 | | 0.1470 |
| | 150 mm-Chamfer45 | | 0.1388 |
| | 100 mm-steeple | | 0.1251 |
| | 150 mm-steeple | | 0.1089 |

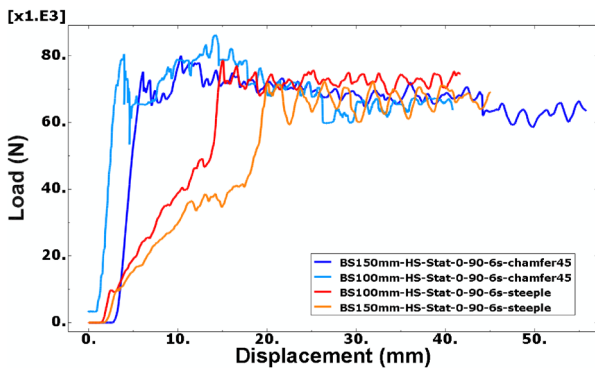


Fig. 21 Load vs displacement experimental results for the QS big-scale Hat-Shape coupons

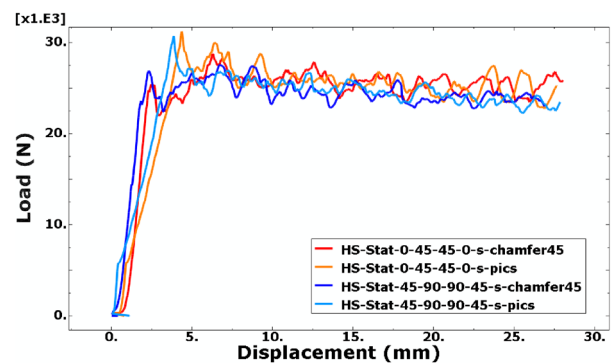


Fig. 22 Load vs displacement experimental results for the QS small-scale Hat-Shape coupons

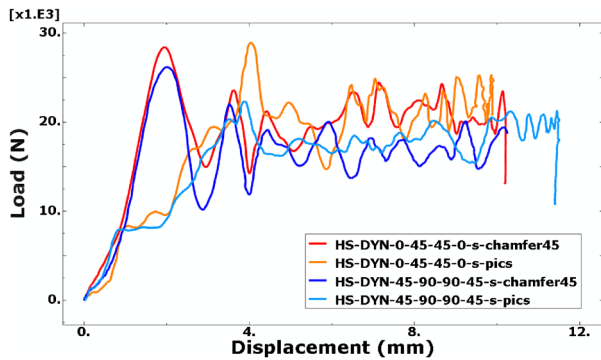


Fig. 23 Load vs displacement experimental results for the Dyn small-scale Hat-Shape coupons

calculated for Hat-Shape and flat-plate coupons tested under QS and low-velocity crushing load. The self-supporting open section geometry Hat-Shape dissipates more energy compared to flat-plate geometry, due to the stress concentration in the corners and the friction between fronds after splaying mode and delamination of external plies.

For the third parameter, the stacking sequence [0/45/45/0]_s seems to improve the specific energy followed, respectively, by the [45/90/90/45]_s and [0/90]2_s layups.

The fourth parameter to be evaluated is the trigger type; corrugated trigger enhances the dissipated energy followed by the steeple, chamfer45° and saw teeth triggers.

The fifth parameter to be investigated is the strain-rate; coupons crushed with low velocity decrease the absorbed energy compared to coupons crushed under QS conditions.

Table 4 presents the accuracy of the UL-Crush material model to predict the SEA for Hat-Shape and flat-plate coupons tested under QS and dynamic crush load conditions.

The material model UL-Crush for flat-plate coupons accurately predict the best material configurations increasing the absorption energy. However, for Hat-Shape coupons, the numerical tool predicts configurations with saw teeth triggers versus configurations with chamfer45° observed with experimental tests. This could be explained by the frictions between big petals or fronds released after delamination of external plies, not already predictable by the new constitutive law.

For flat-plate coupons, the best material configuration in terms of energy absorption is with corrugated trigger and [0/45/45/0]_s stacking sequence; for the composite material with density of 1527 kg/m³, the predicted SEA was approximately 81.009 K Joule/Kg compared to calculated experimental value of 75.049 K Joule/Kg with an error about: 7.36%.

B. Flat-Plate Coupons' Results

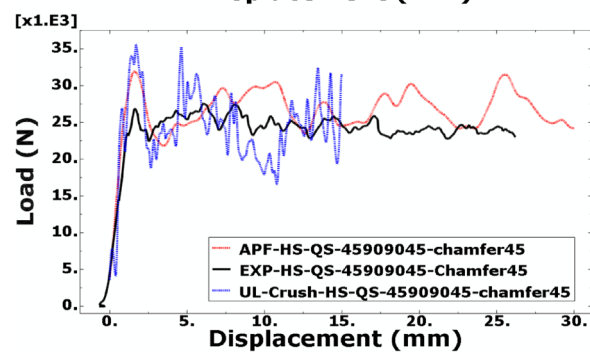
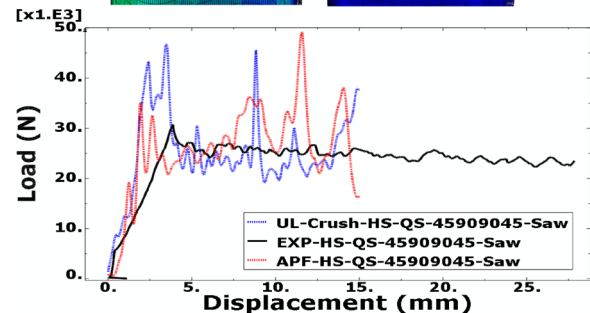
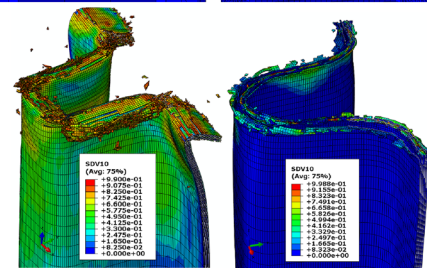
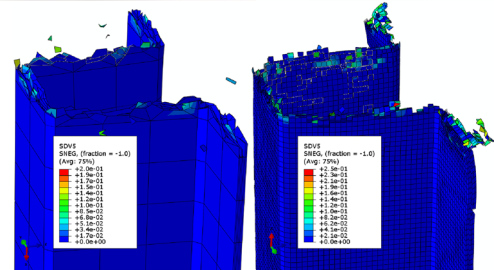
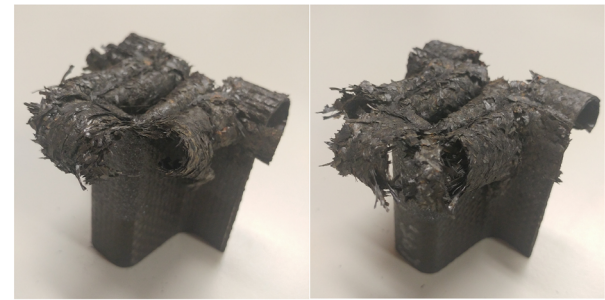


Fig. 24 Comparison between experimental, Abq_Ply_Fabric and UL-Crush QS results for [45/90/90/45]_s Hat-Shape coupons; (left): with saw teeth trigger, (right): with chamfer45 trigger. (SDV5 and SDV10 are the in-plane shear damages)

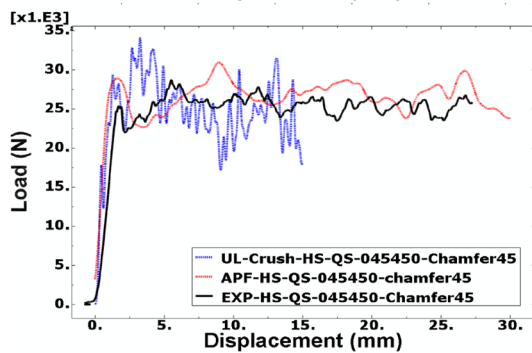
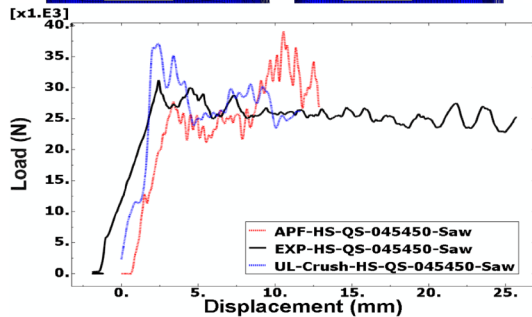
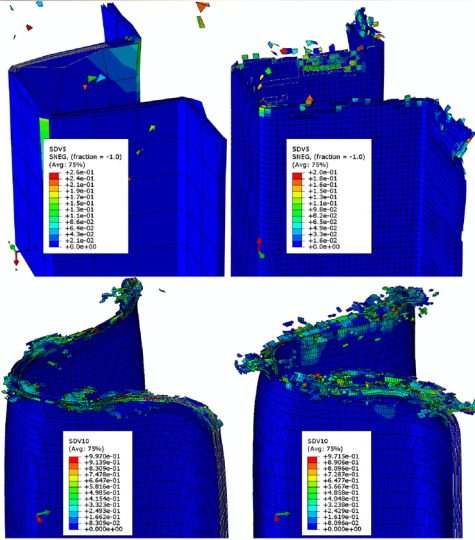


Fig. 25 Comparison between experimental, Abq_Ply_Fabric and UL-Crush QS results for [0/45/45/0]_s Hat-Shape coupons; (left): with saw teeth trigger, (right): with chamfer45 trigger. (SDV5 and SDV10 are the in-plane shear damages)

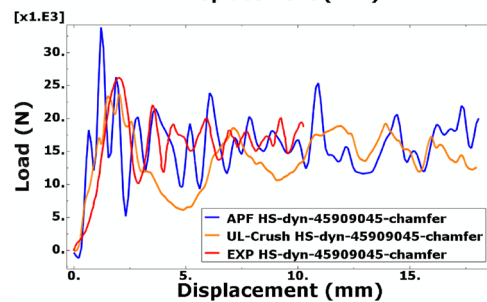
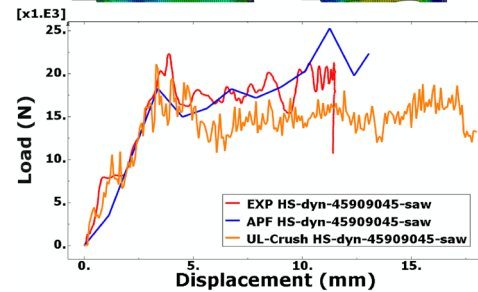
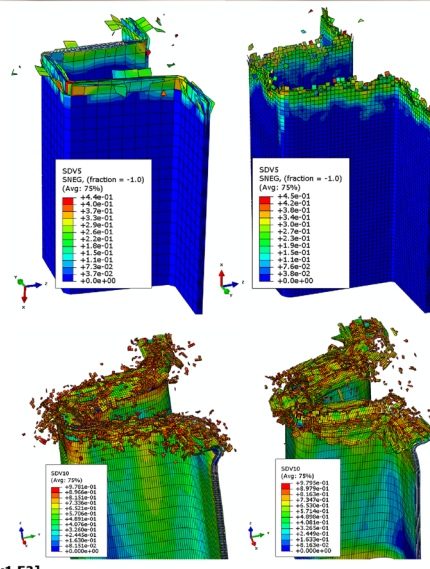
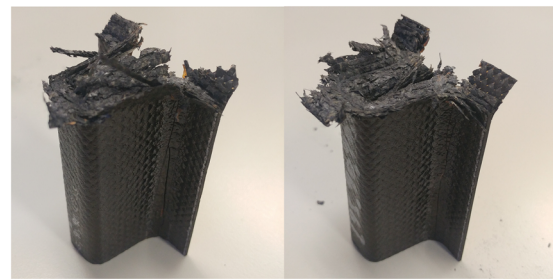


Fig. 26 Comparison between experimental, Abq_Ply_Fabric and UL-Crush Dyn results for [45/90/90/45]_s Hat-Shape coupons; (left): with saw teeth trigger, (right): with chamfer45 trigger. (SDV5 and SDV10 are the in-plane shear damages)

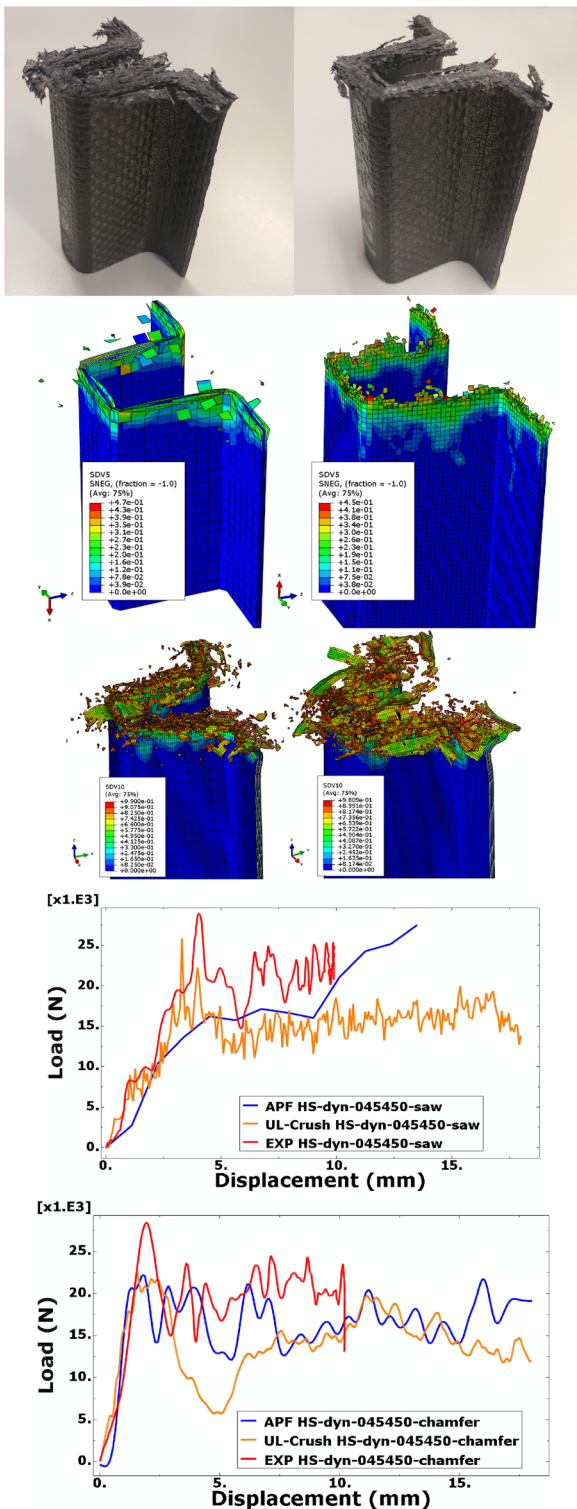


Fig. 27 Comparison between experimental, Abq_Ply_Fabric and UL-Crush Dyn results for [0/45/45/0]_s Hat-Shape coupons; (left): with saw teeth trigger, (right): with chamfer45 trigger. (SDV5 and SDV10 are the in-plane shear damages)

Figures 28, 29, 30, 31, 32, and 33 show a comparison between dynamic and QS experimental and UL-Crush results for crushing of the small-scale flat-plate coupons.

All curves illustrated within Figs. 28, 29, 30, 31, 32, and 33 confirm certainly that flat-plate coupons crushed with low velocity decrease the absorbed energy compared to coupons crushed with QS conditions, due to the disintegration of microstructures.

The long period to reach the steady-state crushing load, (between 3 and 4 mm), for coupons with saw teeth and corrugated trigger types, compared to other coupons with chamfer45° and steeple trigger types, can be partially attributed to the difference of triggers heights, and the time to the fixed steel platen to be in contact with the entire cross-section surface of the specimens.

The crush force efficiency (ratio between peak force and steady-state sustainable load) was approximately one for coupons with corrugated and saw teeth triggers, and less than one for coupons with steeple and chamfer45° trigger types, due to the fast ascendance to the peak force followed by a load drop caused by the splaying crush mode and the delamination of external plies.

The accumulation of debris between delaminated plies and steel rigid wall stiffens the composite coupons and contributes to additional energy absorption resulting in higher steady-state crushing load.

For flat-plate coupons, material model predicts well load vs displacement curves of the crush phenomenon especially for coupons with saw teeth and corrugated trigger types, but splayed external plies have not been accurately predicted due to the elements' deletion and fragmentation formulation adopted, nevertheless, this frond going away from crush front did not participate sufficiently to the accumulated absorbed energy.

For the other coupons with steeple and chamfer45° trigger types, splayed external plies have been clearly released and captured by the new material model, but the steady-state post-peak crushing load have been slightly over- or underestimated due to the contact friction between the fixed steel platen and the fronds.

Table 5 shows a comparison between experimental results and simulation results performed by UL-Crush and Abq_Ply_Fabric material models for Hat-Shape coupons. Numerical results highlighted the capabilities of the new material model to well predict the QS crush behavior of the Hat-Shape cross-section coupons compared to Abq_Ply_Fabric material model, but need more calibrations for dynamic crush behavior; this can be explained by the multitude of damage mechanisms newly introduced in the UL-Crush material model, such as fragmentation, kink-bandings and strain-rate dependency.

Table 4 SEA comparison between UL-Crush and experiments for flat-plate and Hat-Shape coupons

| | Layup | Trigger | Experiments Joule/mm ³ | UL-Crush Joule/mm ³ | | |
|------------------|--------------------|--------------------|--------------------------------------|-----------------------------------|--------|--------|
| FP-QS | [45°/90°/45°/90°]s | Chamfer45° | 0.0935 | 0.1073 | | |
| | | steeple | 0.1145 | 0.0977 | | |
| | | Saw teeth | 0.1000 | 0.0740 | | |
| | | Corrugated | 0.1254 | 0.1154 | | |
| | | [0°/45°/45°/0°]s | Chamfer45° | 0.1146 | 0.1127 | |
| | | | steeple | 0.1264 | 0.1128 | |
| | Saw teeth | | 0.0826 | 0.0733 | | |
| | Corrugated | | 0.1422 | 0.1168 | | |
| | [0°/90°]2 s | | Chamfer45° | 0.1120 | 0.0965 | |
| | | | steeple | 0.1183 | 0.0894 | |
| | | Saw teeth | 0.1094 | 0.1032 | | |
| | | Corrugated | 0.1210 | 0.0952 | | |
| | | FP-Dyn | [45°/90°/45°/90°]s | Chamfer45° | 0.0731 | 0.0749 |
| | | | | steeple | 0.0775 | 0.0777 |
| | Saw teeth | | | 0.0743 | 0.0558 | |
| | Corrugated | | | 0.1003 | 0.0986 | |
| | [0°/45°/45°/0°]s | | | Chamfer45° | 0.0995 | 0.0764 |
| | | | | steeple | 0.0898 | 0.1063 |
| Saw teeth | | | 0.0847 | 0.0543 | | |
| Corrugated | | | 0.1146 | 0.1237 | | |
| [0°/90°]2 s | | | Chamfer45° | 0.0906 | 0.0941 | |
| | | | steeple | 0.0973 | 0.1324 | |
| | Saw teeth | | 0.0763 | 0.0721 | | |
| | Corrugated | | 0.1105 | 0.1259 | | |
| | HS-QS | [45°/90°/45°/90°]s | Chamfer45° | 0.1348 | 0.1403 | |
| | | | Saw teeth | 0.1340 | 0.1449 | |
| Corrugated | | | 0.1374 | 0.1411 | | |
| [0°/45°/45°/0°]s | | Chamfer45° | 0.1367 | 0.1477 | | |
| | | Saw teeth | 0.0911 | 0.0798 | | |
| | | Corrugated | 0.0899 | 0.0796 | | |
| HS-Dyn | [45°/90°/45°/90°]s | Chamfer45° | 0.1081 | 0.0799 | | |
| | | Saw teeth | 0.1002 | 0.0822 | | |
| | [0°/45°/45°/0°]s | Chamfer45° | | | | |
| | | Saw teeth | | | | |

Into front crush zone, kink-bandings' mechanism followed by fragmentation delivers and accumulates debris, and stiffens specimens under compression. When a finer mesh is used, the stiffening behavior is enough to prevent excessive distortion. However, simulation may stop prematurely when the mesh is coarse, but distortion control can be activated in Abaqus/Explicit environment to prevent solid elements from inverting or distorting excessively.

5 Summary and Conclusion

With the advancement made in computational tools combined with coupon level testing, numerical simulations have become unmissable to study and predict crush behavior of

collapsible floor stanchions and beams in aircraft subfloor and cargo structures using a performant simulation tools such as material models.

Due to the simplicity and industrial efficiency, a cost-effective approach with new mesomechanical material model was proposed using homogeneous and anisotropic materials at the level of plies.

The focus was to capture the complex crush damage mechanisms using newly created material model in the scope of development of new aerospace-grade materials with high crush specific energy absorption.

In the present study, Abaqus/Explicit competitive finite-element commercial code was used to implement such new constitutive law user models by VUMAT interface. In total, 60 input parameters and 72 state variables SDV were included.

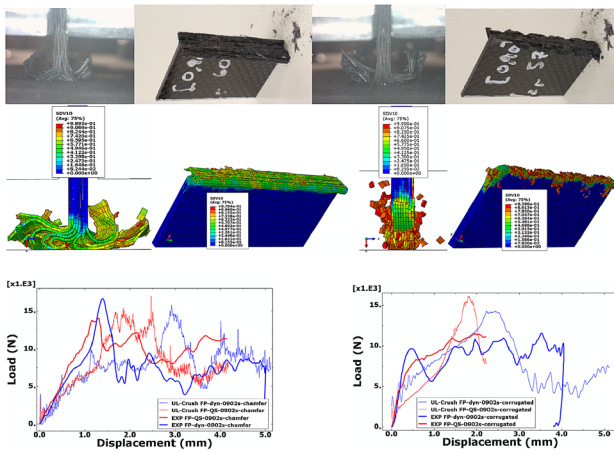


Fig. 28 Flat-plate coupons with $[0/90]_{2s}$ layup: (from left): QS with chamfer45, Dyn with chamfer45, QS with corrugated and Dyn with corrugated (SDV10 is the in-plane shear damage)

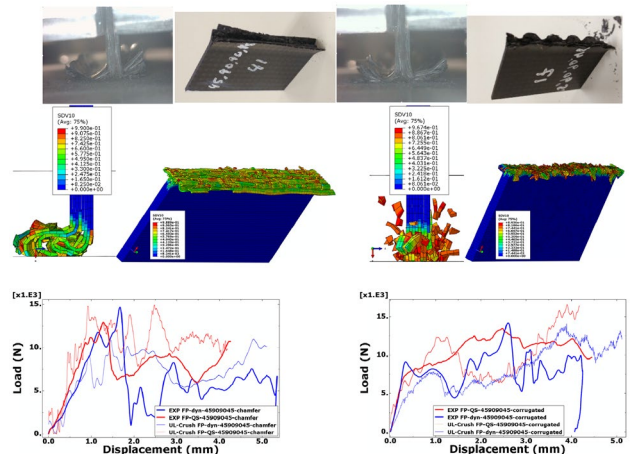


Fig. 30 Flat-plate coupons with $[45/90/90/45]_s$ layup: (from left): QS with chamfer45, Dyn with chamfer45, QS with corrugated and Dyn with corrugated (SDV10 is the in-plane shear damage)

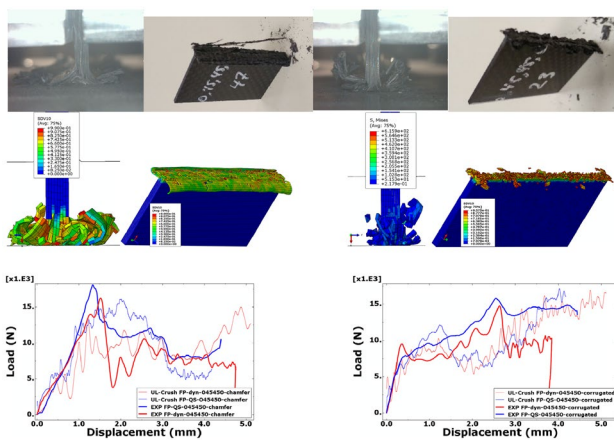


Fig. 29 Flat-plate coupons with $[0/45/45/0]_s$ layup: (from left): QS with chamfer45, Dyn with chamfer45, QS with corrugated and Dyn with corrugated (SDV10 is the in-plane shear damage)

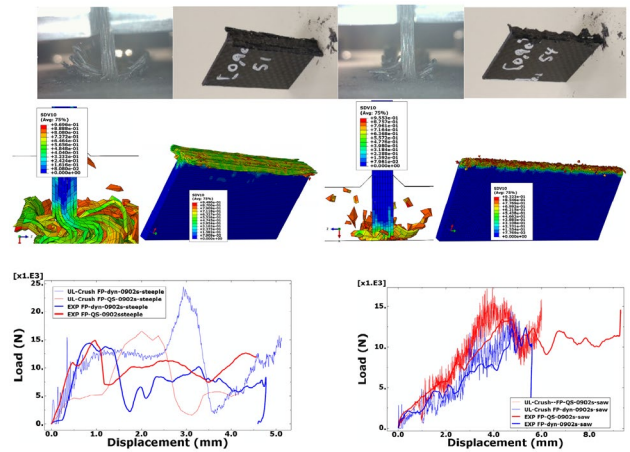


Fig. 31 Flat-plate coupons with $[0/90]_{2s}$ layup: (from left): QS with steeple, Dyn with steeple, QS with saw teeth and Dyn with saw teeth (SDV10 is the in-plane shear damage)

The presented approach could be organized in four main categories: intralaminar modeling, interlaminar modeling, identification procedures and coupon level validation testing.

Concerning the intralaminar modeling, various aspects should be considered: (i) a precise comprehension of the scenario of crush in terms of damage mechanisms sequence, (ii) appropriate representation of each damage mechanism in form of criteria or formulations within constitutive and kinematic laws of the material, and (iii) newly modified Hashin failure initiation criteria, accounting for coupling between different material directions. In addition, with new kink-bandings, criterion and fragmentation formulation have been introduced.

The interlaminar modeling uses cohesive zone CZM approach included in Abaqus/Explicit but comprises some challenges in the definition of the cohesive stiffness and shows some numerical instabilities under coupled and complex loading, input parameters had to be specified precisely to maintain numerical stability.

Regarding the identification procedures, the material model input coefficients are standard tests sufficient, except for Mean Crush Stress (MCS) parameter identifying fragmentation formulation, which can be calculated following newly approach defined in literature.

Finally, coupon level validation uses prepared experimental test plans with CFRP plain weave fabric Hat-Shape self-supporting and flat-plate specimens. To assess the influence of scale dimensions, cross-section geometries, trigger types,

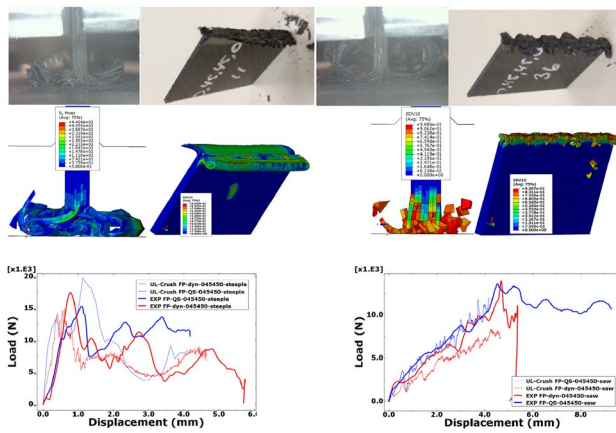


Fig. 32 Flat-plate coupons with $[0/45/45/0]_s$ layout: (from left): QS with steeple, Dyn with steeple, QS with saw teeth and Dyn with saw teeth (SDV10 is the in-plane shear damage)

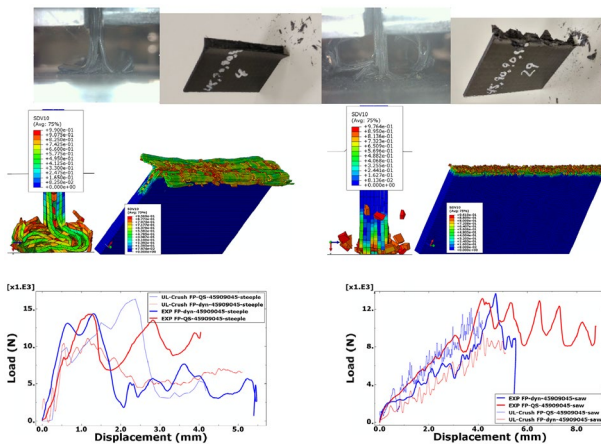


Fig. 33 Flat-plate coupons with $[45/90/90/45]_s$ layout: (from left): QS with steeple, Dyn with steeple, QS with saw teeth and Dyn with saw teeth (SDV10 is the in-plane shear damage)

stacking sequences and strain-rates on the obtained load vs displacement results as well as the specific energy absorption SEA, tests were conducted on new fixtures designed and manufactured specially to prevent catastrophic crushing.

Experimental results showed that the newly designed fixtures include the following features:

- For the flat-plate fixture; it can initiate progressive crushing, without need for complicated anti-buckling systems by optimizing the unsupported height for the flat-plate coupons. Thus, this allows the capturing of the major crush steps (peak force and post-peak sustainable load). As well as the crushing of various specimens' dimensions without standardized limitations of the compression after impact CAI ASTM D7136-37.
- For both, flat-plate and Hat-Shape coupons, fixture is robust for dynamic energies up to 400 Joule and fully incorporated within the CEAST Instron drop tower facility.

It was observed that big dimension scale of coupons might increase the overall absorbed energy. The open cross-section geometry improves dissipation of crush energy by the multiplication of damage mechanisms in the corners and by the friction between delaminated fronds.

The corrugated trigger type enhances the dissipated energy followed by the steeple, chamfer45° and saw teeth trigger types.

For the parameter stacking sequence; the layout $[0/45/45/0]_s$ seems to improve the specific energy because of the high fragmentation capability of the internal 0° plies, followed, respectively, by the $[45/90/90/45]_s$ and $[0/90]_2s$ layouts.

Regarding strain-rate effect, it has been shown that coupons crushed with low velocity decrease the absorbed energy

Table 5 SEA comparison between UL-Crush, Abq_Ply_ Fabric and experiments for Hat-Shape coupons

| Coupons | Layup/trigger | Specific energy absorption (SEA) | | | | |
|---------|--|----------------------------------|------------------------------------|---------|--------------------------------|--------|
| | | Exp Joule/mm ³ | Abq_Ply_ Fab Joule/mm ³ | Error % | UL-Crush Joule/mm ³ | Error% |
| HS-QS | $[45^\circ/90^\circ/45^\circ/90^\circ]_s/\text{chamfer}45^\circ$ | 0.1348 | 0.1524 | 13.06 | 0.1403 | 4.08 |
| | $[45^\circ/90^\circ/45^\circ/90^\circ]_s/\text{saw teeth}$ | 0.1340 | 0.1608 | 20.00 | 0.1449 | 8.13 |
| | $[0^\circ/45^\circ/45^\circ/0^\circ]_s/\text{chamfer}45^\circ$ | 0.1374 | 0.1513 | 10.12 | 0.1411 | 2.69 |
| | $[0^\circ/45^\circ/45^\circ/0^\circ]_s/\text{saw teeth}$ | 0.1367 | 0.1579 | 15.51 | 0.1477 | 8.05 |
| HS-Dyn | $[45^\circ/90^\circ/45^\circ/90^\circ]_s/\text{chamfer}45^\circ$ | 0.0911 | 0.0915 | 14.63 | 0.0798 | 12.43 |
| | $[45^\circ/90^\circ/45^\circ/90^\circ]_s/\text{saw teeth}$ | 0.0899 | 0.0919 | 15.33 | 0.0796 | 11.42 |
| | $[0^\circ/45^\circ/45^\circ/0^\circ]_s/\text{chamfer}45^\circ$ | 0.1081 | 0.0937 | 17.23 | 0.0799 | 26.09 |
| | $[0^\circ/45^\circ/45^\circ/0^\circ]_s/\text{saw teeth}$ | 0.1002 | 0.0983 | 19.51 | 0.0822 | 17.91 |

due to the disintegration of the microstructure compared to coupons crushed under QS conditions.

In general, most effects of crush were captured by the new material model and this approach identified an acceptable agreement between simulations and test results over a large wide range of material configurations' coefficients, providing an added value and a new basis for industrials and R&D laboratories for further developments.

Acknowledgements The authors declared no potential conflicts of interest with respect to the research, authorship, and/or publication of this article. The authors would like to thank the Natural Science and engineering Research Council of Canada (NSERC), Consortium for research and innovation in aerospace in Quebec (CRIAQ) through CRIAQ Project COMP-410, Bombardier Aerospace and Bell Helicopter Textron Company (BHTC) for funding, technical support and materials.

References

1. Tabiei, A., Medikonda, S.: A non-linear strain-rate micro-mechanical composite material model for impact problems. In: 15th International LS-DYNA Users Conference, Detroit, 10–12 June 2018, pp 1–22 (2018)
2. Palma, L.D., Caprio, F.D., Chiariello, A., Ignarra, M., Russo, S., Riccio, A., Luca, A.D., Caputo, F.: Vertical drop test of composite fuselage section of a regional aircraft. *AIAA J.* **58**(1), 474–487 (2020)
3. Caputo, F., Lamanna, G., Perfetto, D.: Experimental and numerical crashworthiness study of a full-scale composite fuselage section. *AIAA J.* (2020). <https://doi.org/10.2514/1.J059216>
4. Fasanella, E.L., Jackson, K.E.: Best practices for crash modeling and simulation. In: Technical Memorandum: NASA/TM-2002-211944, Ref. ARL-TR-2849 (2002)
5. McGregor, C.J.: Simulation of progressive damage development in braided composite tubes under axial compression. Master's thesis, University of British Columbia, Vancouver (2005)
6. Lombarkia, R., Gakwaya, A., Nandlall, D., Dano, M.-L., Lévesque, J., Benkhelifa, A., Vachon-Joannette, P., Gagnon, P.: A meso-mechanical material model describing a crash behavior of 2D plain weave fabric composites. *CEAS Aeronaut. J.* (2021). <https://doi.org/10.1007/s13272-020-00488-1>. (Published online: 04 Jan 2021)
7. Guida, M., Marulo, S.A.F.: Advances in crash dynamics for aircraft safety. *Prog. Aerosp. Sci.* **98**, 106–123 (2018)
8. Delsart, D., Portement, G., Waimer, M.: Crash testing of a CFRP commercial aircraft sub-cargo fuselage section. *Struct. Integr. Proc.* **2**, 2198–2205 (2016)
9. Saito, K., Nishi, M.: FE Modeling to simulate the axial crushing behavior of DFRP composites. In: 21st International Conference on Composite Materials, Xian, 20–25 August 2017
10. Chiu, L.N., Falzon, B.G., Boman, R., Chen, B., Yan, W.: Finite Element modeling of composite structures under crushing load. *Compos. Struct.* **131**, 215–225 (2015)
11. Bednarczyk, B.A., Stier, B., Simon, J.-W., Reese, S., Pineda, E.J.: Meso- and micro-scale modeling of damage in plain weave composites. *Compos. Struct.* **121**, 258–270 (2015)
12. McGregor, C., Navid Zobeiry, R.V.: A constitutive model for progressive compressive failure of composites. *J. Compos. Mater.* **42**(25), 2687–2716 (2008)
13. Janapala, N.R., Chang, F.-K., Goldberg, R.K., Roberts, G.D., Jackson, K.E.: Crashworthiness of composite structures with various fiber architectures. In: 11th International LS-DYNA® Users Conference, Detroit, USA (2010)
14. Cox, N.B., Flanagan, G.: Handbook of analytical methods for textile composites. NASA Contractor Report No: 4750 (1997)
15. Kashani, M.H., Milani, A.S.: Damage prediction in woven and non-woven fabric composites. In: Jeon, H.Y. (eds.) *Non-Woven Fabrics*, pp. 234–262. INTECH (2016)
16. Ghane, E., Mohammadi, B.: Entropy-damage mechanics for the failure investigation of plain weave fabric composites. *Compos. Struct.* **250**, 1–13 (2020). <https://doi.org/10.1016/j.compstruct.2020.112493>
17. Joosten, M., Dutton, S., Kelly, D., Thomson, R.: Experimental and numerical investigation of the crushing response of an open section composite energy absorbing element. *Compos. Struct.* **93**, 682–689 (2011)
18. Esnaola, A., Elguezabal, B., Aurrekoetxea, J., Gallego, I., Ulacia, I.: Optimization of the semi-hexagonal geometry of a composite crush structure by finite element analysis. *Compos. Part B* **93**, 56–66 (2016)
19. Waimer, M., Siemann, M., Feser, T.: Simulation of CFRP components subjected to dynamic crash loads. *Int. J. Impact Eng.* **101**, 115–131 (2017)
20. Rosen, V.W.: Mechanics of composite strengthening. In: *Fiber Composite Materials*, Seminar of the American Society for Metals, pp. 37–75. Metals Park, Ohio (1965)
21. Argon, A.S.: Fracture of composites. In: *Treatise on Materials Science and Technology*, vol. 1, pp. 79–114. Academic Press, New York (1972)
22. Pinho, S., Dávila, C., Camanho, P., Iannucci, L., Robinson, P.: Failure models and criteria for frp under in-plane or three-dimensional stress states including shear non-linearity. In: Technical Memorandum: NASA/TM-2005-213530, Hanover (2005)
23. Rivallant, S., Israr, H., Barrau, J.: Modélisation par éléments finis de l'écrasement de stratifiés d'unidirectionnels carbone/époxy à faible vitesse. In: JNC 18 - 18èmes Journées Nationales sur les Composites, Nantes, France, 12–14 June 2013
24. Akil, O., Yildirim, U., Guden, M., Hall, I.W.: Effect of the strain-rate on the compression behavior of woven fabric S2-glass fiber reinforced vinyl ester composite. *Polym. Test.* **22**(8), 883–887 (2003)
25. Gilat, A., Goldberg, R.K., Roberts, G.D.: Experimental study of strain-rate dependant behavior of carbon epoxy composite. *Compos. Sci. Technol.* **62**, 1469–1476 (2002)
26. Tay, T.E., Ang, H.G., Shim, V.W.: An empirical strain-rate dependant constitutive relationship for glass fiber reinforced epoxy and pure epoxy. *Compos. Struct.* **33**(4), 201–210 (1995)
27. Li, Z., Lambros, J.: Strain-rate effects on the thermomechanical behavior of polymers. *Int. J. Solids Struct.* **38**, 3549–3562 (2001)
28. Krasnobrizha, A., Rozycki, P., Gornet, L., Cosson, P.: Hysteresis behavior modeling of woven composite using a collaborative elastoplastic damage model with fractional derivatives. *Compos. Struct.* **158**, 101–111 (2016)
29. Glodberg, R.K., Roberts, G.D., Gilat, A.: Implementation of an associative flow rule including hydrostatic stress effects into the high strain-rate deformation analysis of polymer matrix composites. *J. Aerosp. Eng.* **18**(1), 18–27 (2005)
30. Welsh, L., Harding, J.: Effect of strain-rate on the tensile failure of woven reinforced polyester resin composites (1985). <https://hal.archives-ouvertes.fr/jpa-00224782>. Accessed 19 Oct 2021
31. Jendli, Z., Fitoussi, J., Bocquet, M., Walrick, J.C.: Strain-rate effects on the mechanical behavior of carbon-thermoplastic matrix woven composites. In: *Comptes Rendus des JNC 18 - ÉCOLE CENTRALE NANTES*, 12-14 June 2013, Nantes (2013)
32. Armattoe, K.M., Roycki, P., Mbacke, M.: Numerical and experimental characterization of the hygrothermal and strain-rate

- dependant behavior of woven glass fiber reinforced polyamide. In: ECCM17—17th European Conference on Composite Materials, Munich, (2016)
33. Feld, N., Coussa, F., Delattre, B.: A novel approach for the strain-rate dependent modelling of woven composites. *Compos. Struct.* **192**, 568–576 (2018)
 34. Schaefer, J.D., Daniel, I.M.: Strain-rate-dependent yield criteria for progressive failure analysis of composite laminates based on the northwestern failure theory. *Exp. Mech.* **58**, 487–497 (2018). <https://doi.org/10.1007/s11340-017-0366-z>
 35. Yen, C.F.: Ballistic impact modeling of composite materials. In: Proceedings of the 7th International Ls-Dyna User Conference, DYNAllook, vol. 6, pp. 15–26. Dearborn (2002)
 36. Zheng, X., Binenda, W.K.: Rate dependent Shell element composite material model implementation. *J. Aerosp. Eng.* **21**(3), 140–151 (2008)
 37. Donadon, M., Frascino, S., Mariano, A., Arbelo, A., Faria, R.A.: A Three-dimensional ply failure model for composite structures. *Int. J. Aerosp. Eng.* **2009**, 486063 (2009). <https://doi.org/10.1155/2009/486063>
 38. Ming, L., Pantalé, O.: An efficient and robust VUMAT implementation of elastoplastic constitutive laws in Abaqus/Explicit finite element code. *Mech. Ind.* **19**(3), 308 (2018). <https://doi.org/10.1051/meca/2018021>
 39. Beckelyncq, B.: Étude de la délamination sur des matériaux composites tissés taffetas: Essais de caractérisation et simulations numériques. Université Laval, Québec (2016)
 40. Salvi, A.G., Waas, A.M.: Rate-dependant compressive behavior of unidirectional carbon fiber composites. *Polym. Compos.* **25**(4), 397–406 (2004)
 41. Zhou, J., Guan, Z., Cantwell, W.: Modelling compressive crush of composite tube reinforced foam sandwiches. In: International Conference on Composite Materials ICCM, Cambridge, England, 28–30 July 2014 (2014)
 42. Lombarkia, R., Gakwaya, A., Nandlall, D., Dano, M.-L., Lévesque, J., Vachon-Joannette, P.: Experimental investigation and finite-element modeling of the crushing response of hat shape open section composites. *Int. J. Crashworth.* (2020). <https://doi.org/10.1080/13588265.2020.1838773>
 43. SIMULIA: Abaqus Documentations. Dassault Systems, 6.14 (2014)
 44. SIMULIA: Abaqus Documentations. Dassault Systems (2020)
 45. Lombarkia, R., Gakwaya, A., Nandlall, D., Dano, M.L., Lévesque, J., Vachon-Joannette, P., Gagnon, P., Benkhelifa, A.: Comparative study of energy absorption capability of flat plate coupons made by CFRP plain weave fabric composites. *World J Mech* **11**, 121–145 (2021). <https://doi.org/10.4236/wjm.2021.117010>
 46. Israr, H., Rivallant, S., Barrau, J.: Experimental investigation on mean crushing stress characterization of carbon–epoxy plies under compressive crushing mode. *Compos. Struct.* **96**, 357–364 (2013)

Publisher's Note Springer Nature remains neutral with regard to jurisdictional claims in published maps and institutional affiliations.